Volume 10
Number 39
21 October 2022
Pages 7887–8102

Journal of Materials Chemistry B

Materials for biology and medicine

rsc.li/materials-b

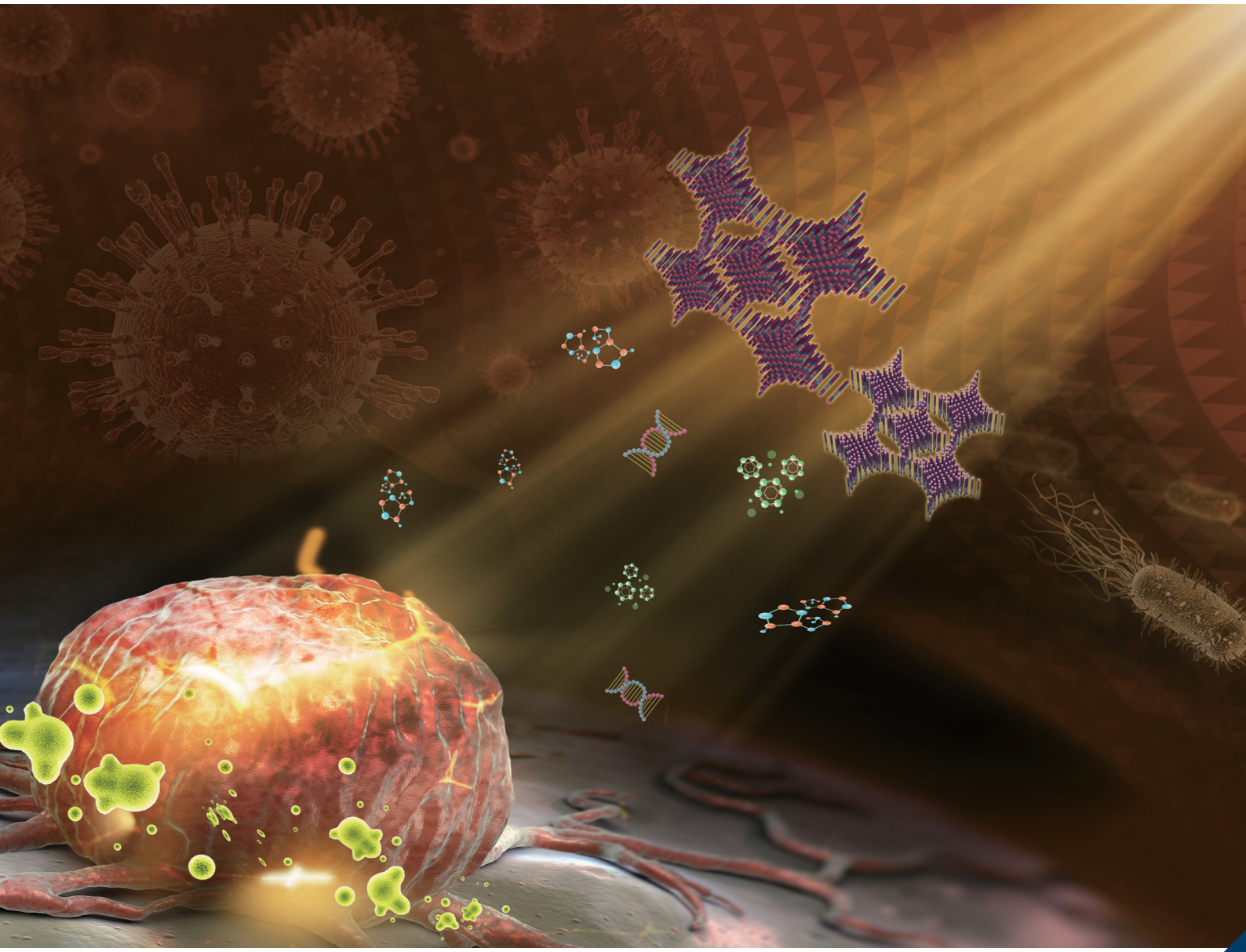

ISSN 2050-750X

PAPER

Wei Tan, Baolong Zhou *et al.*
A diselenium-bridged covalent organic framework with pH/GSH/photo-triple-responsiveness for highly controlled drug release toward joint chemo/photothermal/chemodynamic cancer therapy

ROYAL SOCIETY OF CHEMISTRY

Indexed in Medline!

Journal of Materials Chemistry B

ROYAL SOCIETY OF CHEMISTRY

PAPER

View Article Online
View Journal | View Issue

Cite this: J. Mater. Chem. B, 2022, 10, 7955

A diselenium-bridged covalent organic framework with pH/GSH/photo-triple-responsiveness for highly controlled drug release toward joint chemo/photothermal/chemodynamic cancer therapy†

Han Lou,‡[ad] Lichao Chu,‡[b] Wenbin Zhou,‡[d] Jinli Dou,[a] Xiaotong Teng,[c] Wei Tan*[c] and Baolong Zhou*[a]

Received 11th May 2022,
Accepted 19th June 2022

DOI: 10.1039/d2tb01015a

rsc.li/materials-b

Here, a novel joint chemo/photothermal/chemodynamic therapy was developed using a pH/GSH/photo triple-responsive 2D-covalent organic framework (COF) drug carriers for passive target treatment of tumors with extraordinarily high efficiency. The well-designed COF (DiSe-Por) with simultaneous dynamic diselenium and imine bonds, synthesized by the copolymerization of 4,4′-diselanediyldibenzaldehyde (DiSe) with 5,10,15,20-(tetra-4-aminophenyl)-porphyrin (Por) *via* Schiff base chemistry, which was applied as the host for effective encapsulation and highly controlled release of anticancer drug (DOX), was stable under normal physiological settings and can effectively accumulate in tumor sites. After being internalized into the tumor cells, the unique microenvironment *i.e.*, acidic pH and overexpressed GSH, triggered substantial degradation of DiSe-Por-DOX, promoting DOX release to kill the cancer cells. Meanwhile, the breaking of Se–Se bonds boosted the generation of intracellular ROS, disturbing the redox balance of tumor cells. The highly extended 2D structure endowed the drug delivery system with significant photothermal performance. The rise of temperature with external laser irradiation (808 nm) further promoted drug release. Additionally, the phototherapy effect was further augmented after the loading of DOX, guaranteeing an almost complete drug release to tumor tissue. As a result, the triple-responsive drug delivery system achieved a synergistic amplified therapeutic efficacy with a growth inhibitory rate of approximately 93.5% for the tumor xenografted in nude mice. Moreover, the body metabolizable and clearable DiSe-Por-DOX presented negligible toxicities toward major organs *in vivo*. All these characteristics verified the great potential of DiSe-Por-DOX nanosheets for multi-modality tumor treatment, accelerating the application range of COFs in biomedical fields.

Introduction

As one of the leading causes of human death, cancer has always been a major clinical challenge.[1] Hitherto, various modalities, including chemotherapy, gene therapy, radiotherapy, phototherapy, and immunotherapy, are developed for cancer treatment and great advances have been made in clinical outcomes for patients.[2–6] Chemotherapy, involving the usage of chemical drugs, is widely used in clinics for the treatment of a variety of cancers.[7–9] However, the clinical application of mono chemotherapy is seriously hampered by its unsatisfactory efficacy against drug-resistant cancers, as well as its severe side effects caused by the poor selectivity to cancerous tissue over normal tissues.[10,11]

As a novel modality for cancer treatment, chemodynamic therapy (CDT) exhibits preferable therapeutic performance and satisfying biosafety. In comparison with traditional therapies, CDT can generate spatiotemporal controllable and tissue depth-unlimited reactive oxygen species (ROS) in response to the high level of hydrogen peroxide (H_2O_2) in the TME. Recent

[a] School of Pharmacy, Weifang Medical University, Weifang, 261053, Shandong, P. R. China. E-mail: zhoubaolong@wfmc.edu.cn
[b] Department of Anesthesiology, The First Affiliated Hospital of Weifang Medical University (Weifang People's Hospital), Weifang, 261031, Shandong, P. R. China
[c] Department of Respiratory Medicine, The First Affiliated Hospital of Weifang Medical University (Weifang People's Hospital), Weifang, 261031, Shandong, P. R. China
[d] Department of Urology, Affiliated Hospital of Weifang Medical University, Weifang Medical University, Shandong, P. R. China

† Electronic supplementary information (ESI) available. See DOI: https://doi.org/10.1039/d2tb01015a

‡ These authors contribute equal to this article.

reports have validated that cancer therapy in combination with two or more modalities, could not only significantly improve the therapeutic potency of cancer cells, but also reduce the adverse side effects to the body, greatly.[12–15] The main challenge of the combinatorial therapies relies on how to engineer two or more different therapies into one smart platform, maximizing their effectiveness.[16,17]

The specific tumor microenvironments (TME), including hypoxia, low pH value, and overproduction of hydrogen peroxide, offer the potential for new therapies.[18,19] Given that, numerous carriers have been developed, including both the synthetic (*e.g.* metal–organic frameworks and porous organic polymer)[20,21] and natural carriers (*i.e.* exosomes and liposomes),[22,23] which are used as multifunctional therapeutic platforms for joint cancer therapy.[24,25] Covalent–organic frameworks (COFs) are emerging multifunctional materials linked by dynamic covalent bonds, which have attracted considerable attention in recent years.[26,27] The programmable preparation process endowed the COFs with a tailored structure and function, as well as unique electronic and photochemical properties, which have presented great potential for biomedical application.[28] Meanwhile, the dynamic covalent linkage of COFs could realize controlled drug release, boosting anticancer therapeutic effects.[29] Nevertheless, the high bond energy of covalent linkages, especially imine, render an insufficient response to tumor microenvironments, which is not adequate for effective control of drug release, preventing complete drug release.[30,31] Therefore, it is very necessary to achieve complete drug release, maximizing the effectiveness of combination therapy.

Compared with normal tissues, tumor tissues feature a specific physical microenvironment, including high levels of intracellular glutathione (GSH) and acidic pH, which offers a platform for the development of a novel drug carrier.[32] Inspired by this, a diselenium-bridged porphyrin-based covalent organic framework (DiSe-Por-DOX) with pH/GSH/photo-triple-sensitive was facilely prepared by Schiff-base chemistry between 5,10,15,20-(tetra-4-aminophenyl)porphyrin (Por) and 4,4′-diselanediyldibenzaldehyde (DiSe), which could be applied as a host for the efficient loading of doxorubicin (DOX). The coexistence of diselenium and imine bonds endowed DiSe-Por-DOX with unique passive targeting release performance. After internalization into tumor cells, DiSe-Por-DOX was degraded gradually, releasing the encapsulated DOX in response to the unique TME. The breaking of Se–Se bonds exerted chemodynamic therapy by boosting the generation of intracellular ROS, breaking the redox balance in cancer cells.[33] Compared with the pure Por block, due to the highly extended two-dimensional structure, the porous carrier showed a significantly enhanced photothermal performance.[34] The rise of temperature accelerated the movement of drug molecules, thereby further promoting the diffusion of the drug from the materials.[35] Owing to the multi-responsive characteristics, the DiSe-Por-DOX drug delivery system realized an almost complete drug release at the tumor sites, maximizing the synergistic chemo/photothermal/chemodynamic therapeutic effects. This work demonstrated the great potential of COFs for target drug delivery and combination cancer therapy, which would accelerate the application range of COFs in biomedical fields.

Results and discussions

As seen from Scheme 1, the diselenium-bridged porphyrin-based covalent organic framework (DiSe-Por) was prepared by the copolymerization of 5,10,15,20-(tetra-4-aminophenyl) porphyrin (Por) and 4,4′-diselanediyldibenzaldehyde (DiSe) *via* the acetic-acid-catalyzed Schiff-base chemistry. And the DiSe-Por-DOX composite was obtained by the self-assembly strategy *via* physical absorption, hydrogen-bond, and π–π stacking interactions. And the details are given in the synthetic section.

As shown in Fig. 1(A), the Fourier transform infrared spectroscopy (FTIR) of DiSe-Por integrates the features of both starting materials, from which characteristic absorption bands of DiSe at 1635 cm^{-1} (C=C bond), 1134 cm^{-1} (Ar–H vibration of benzene), 833 cm^{-1} (Se–Se bond), and 584 cm^{-1} (Se–C bond)[36–38] and Por (skeleton stretching vibration of pyrrole at 1470 cm^{-1} and benzene at 1600 cm^{-1}, bending vibrations of the N–H bond and deformation vibrations of the C–H bond of the macrocycle tetrapyrrole sections at 3210 cm^{-1} and 1510 cm^{-1}, respectively)[39] could be simultaneously observed. In addition, a strong vibration peak at 1610 cm^{-1} ascribed to the polymerization of amine and aldehyde appeared, demonstrating the total consumption of building blocks.[40] Apart from the peaks of DiSe-Por, obvious absorption peaks of DOX at 2930 and 1623 cm^{-1} could also be detected from the FT-IR of DiSe-Por-DOX.[41]

As verified by thermogravimetric analysis (TGA) in Fig. 1(C), DiSe-Por featured excellent thermal stability up to 300 °C. Afterwards, owing to the decomposition of porous networks, a gradual loss of 36% was found at 800 °C. Whereas, the TGA of DiSe-Por-DOX combined the feature of DiSe-Por and DOX, simultaneously. Similar to DOX, a drastic weight loss at 200–280 °C, ascribed to the thermal decomposition of encapsulated DOX, could be detected from the TGA of DiSe-Por-DOX.[42] As shown in Fig. 1(D), the characteristic X-ray diffraction (XRD) peaks of DOX (12.9, 14.7, 16.4, 18.3, 19.3 and 20.5°) almost disappeared in DiSe-Por-DOX, demonstrating that the majority of drugs are well-loaded inside DiSe-Por.[43] Transmission electron microscopy (TEM) images in Fig. 1(E) revealed the sheet-like morphology of the as-synthesized DiSe-Por, which was well retained after the loading of DOX, demonstrating that DiSe-Por was an ideal vector for the encapsulation of drugs. EDS elemental mapping (Fig. S3 and S4, ESI†) verified the homogeneous distributions of Se, N and C in the porous skeleton. The porosity of DiSe-Por and DiSe-Por-DOX was estimated by the low temperature N_2 uptake measurements at 77 K. As seen in Fig. 1(F), DiSe-Por showed a typical type-IV reversible isotherm, with a vertical adsorption increase in the low pressure range ($P/P_0 < 0.01$) coupled with a big hysteresis loop similar to 2D graphene at the branch of the adsorption/desorption curve, indicative of the coexistence of micropores and mesopores.[44] In addition, a rapid uptake increase appeared again in the high-pressure range

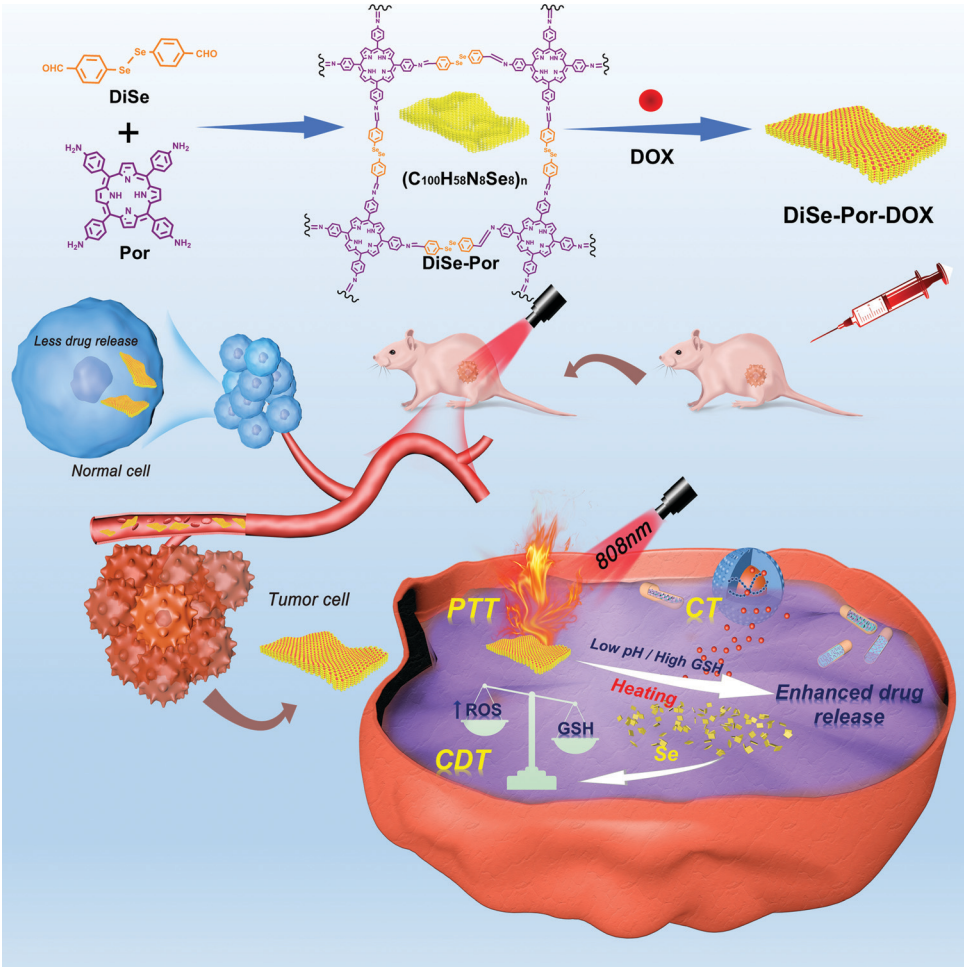

Scheme 1 Schematic illustration of the DiSe-Por-DOX, drug delivery, and *in vivo* combination antitumor therapy.

(P/P_0 > 0.8), revealing the coexistence of macropores.[45,46] However, the micropores almost disappeared for the DiSe-Por-DOX sample, which could be ascribed to the loading of DOX inside COF, blocking the micropore.[47] The surface area of DiSe-Por using the BET model was calculated to be 73.5 $m^2 g^{-1}$, but it decreased to 7.9 $m^2 g^{-1}$ for the DiSe-Por-DOX. The much lower surface area of DiSe-Por-DOX indicated the loading of DOX into the porous networks. The hierarchical pore structure could also be intuitively observed from the Barret–Joyner–Halenda (BJH) and Horvaih–Kawazoe (HK) plot pore size distribution (PSD) curve. As seen in Fig. 1(G), clear peak signals ranging from mesopores to macropores could be observed for both DiSe-Por and DiSe-Por-DOX. Agreeing well with the BET result, the micropore in DiSe-Por almost disappeared after the encapsulation of DOX. The details of the porosity are listed in Table S1 in the ESI.† The DOX loading capacity (LC) reached 35.12% for DiSe-Por-DOX at a mass ratio (material : drug) of 1 : 2. And the details are given in Table S2 (ESI†).

Photothermal property evaluation of vectors *in vitro*

The photothermal effect was initially evaluated in the aqueous dispersion of various materials under bio-friendly near-Infrared (NIR) laser irradiation (808 nm for 6 min), which is widely used for biomedical applications with a strong tissue penetration capacity.[48] The vis-NIR absorbance spectra (Fig. 1(B)) clearly revealed that both DiSe-Por and DiSe-Por-DOX possessed desired absorption in the NIR-I region (700–850 nm), and the loading of DOX increased the NIR absorbance, greatly. The slight enhancement of the DiSe-Por-DOX absorption peak could be attributed to the decrease of the orbital energy difference caused by the π–π stacking of the loaded electron-deficient DOX, which led to the increase of the molar absorption coefficient, as well as the slight increase of the UV absorption.[49] As displayed in Fig. 2(A), upon laser irradiation (1.5 W cm^{-2}) for 6 min, DiSe-Por dispersions showed an obvious temperature increase of 27.9 °C, much higher than the pure Por (10.2 °C), but lower than that of DiSe-Por-DOX (33.0 °C) at the same concentration of DiSe-Por. The excellent photothermal activity could be ascribed to the joint action of the highly extended two-dimensional structure of the COF carrier with the loading of DOX in the porous skeleton, which was in favor of heat conduction.[50] The temperatures of DiSe-Por and DiSe-Por-DOX dispersion gradually increased in a manner that depended on both the power density (Fig. 2(B) and (C)) and concentration (Fig. 2(D) and (E)). A higher illumination power density and dispersion concentration lead to a higher temperature increase.

At a DiSe-Por concentration of 600 μg mL^{-1}, the temperature increase varied from 36.3 to 57.1 °C for pure DiSe-Por (*vs.* 36.3–65.2 °C for DiSe-Por-DOX) with the increase of the power density from 0.5 to 2.0 W cm^{-2}. Meanwhile, at a constant power density of 1.5 W cm^{-2}, there was a positive correlation between the heating rate and concentration of DiSe-Por and DiSe-Por-DOX. The heating rate of DiSe-Por-DOX was obviously better than DiSe-Por at an identical laser power. For example, under identical conditions (600 μg mL^{-1}, 1.5 W cm^{-2}), the temperature of DiSe-Por-DOX increased to 59.5 °C, which was higher than that of DiSe-Por (54.5 °C). As depicted in Fig. 2(F), after five consecutive on-off cycles, the temperature variation curves showed no obvious changes, indicating a good photostability of DiSe-Por-DOX.[51] Furthermore, the photothermal conversion efficiency of DiSe-Por-DOX *via* monitoring the heating and cooling process was calculated to be 24.59%. And the details are given in the ESI.† A thermal imaging camera was used to visualize the temperature change of DiSe-Por and DiSe-Por-DOX. One can see clearly from Fig. 2(I) that under laser irradiation (1.5 W cm^{-2}), both the DiSe-Por and DiSe-Por-DOX gradually gave bright thermal images within 6 minutes. Whereas, the thermal images of DiSe-Por-DOX were brighter than pure DiSe-Por.

In vivo drug release behavior

The multiple stimuli-responsive drug release behavior of as-synthesized materials was initially evaluated under acidic and/or oxidative conditions with/without laser irradiation (808 nm) *in vitro*. As seen from Fig. 3(A), after continuous incubation for 96 hours, only about 27.9% of DOX was released in the neutral environment (pH 7.4), whereas, the cumulative release amount reached 42.4% and 61.3%, at pH values of 6.5 and 5.5, respectively. Such a consequence revealed a prominent acid-responsive release behavior of DiSe-Por-DOX. As expected, the release of DOX increased with the increase of the GSH concentration (0.1 mM to 10 mM). Previous reports verified that diselenide bonds were easily reduced to selenol by the highly

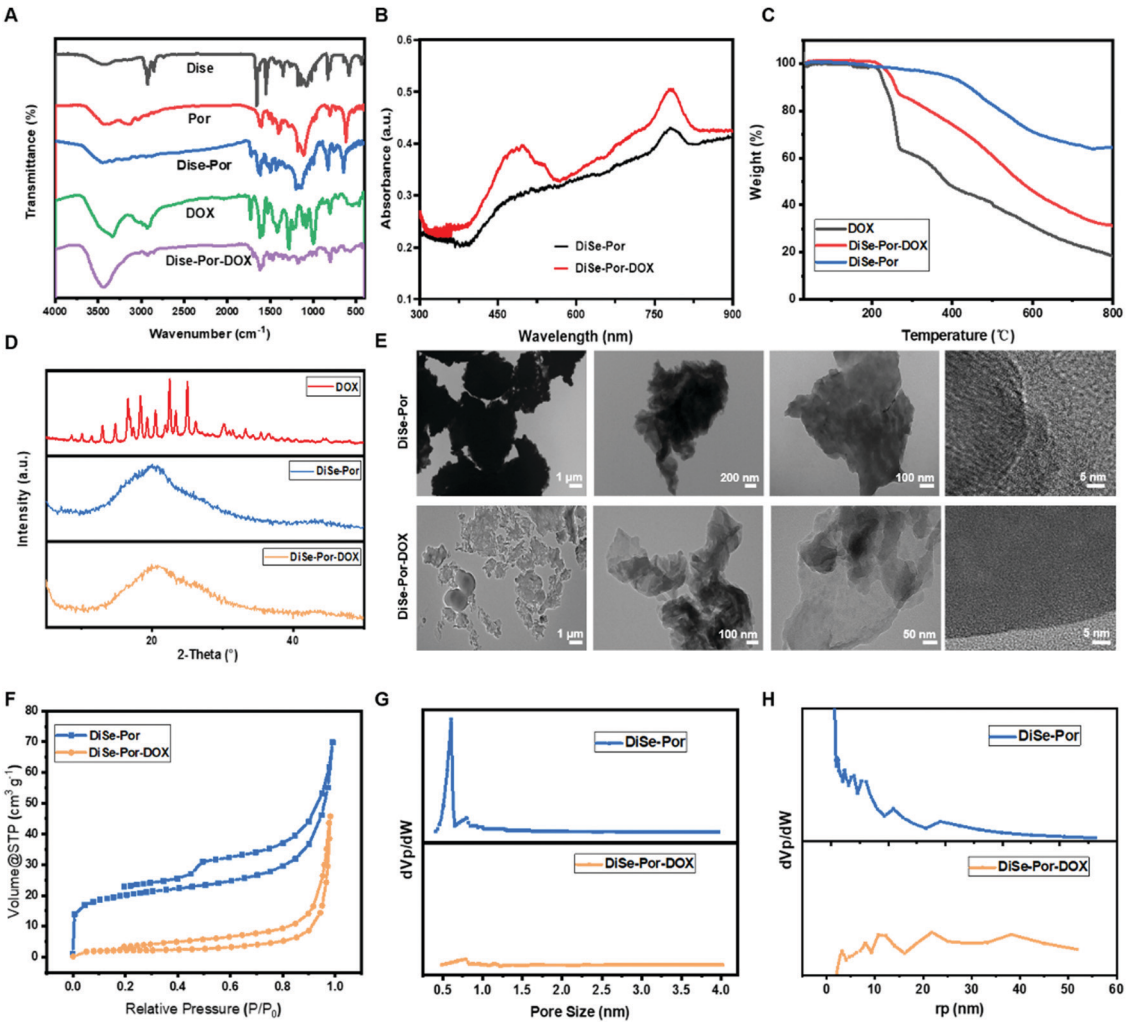

Fig. 1 (A) FT-IR spectrum of DiSe, Por, DiSe-Por, DOX, and DiSe-Por-DOX. (B) UV-Vis-NIR absorbance spectra of DiSe-Por and DiSe-Por-DOX. (C) TG of the prepared samples. (D) Powder XRD of the prepared samples and DOX. (E) TEM of DiSe-Por and DiSe-Por-DOX at different scale bars, respectively. (F) Powder XRD of prepared samples and DOX. (G) BJH-plot PSD curve of DiSe-Por and DSe-Por-DOX. (H) HK-plot PSD curve of DiSe-Por and DiSe-Por-DOX.

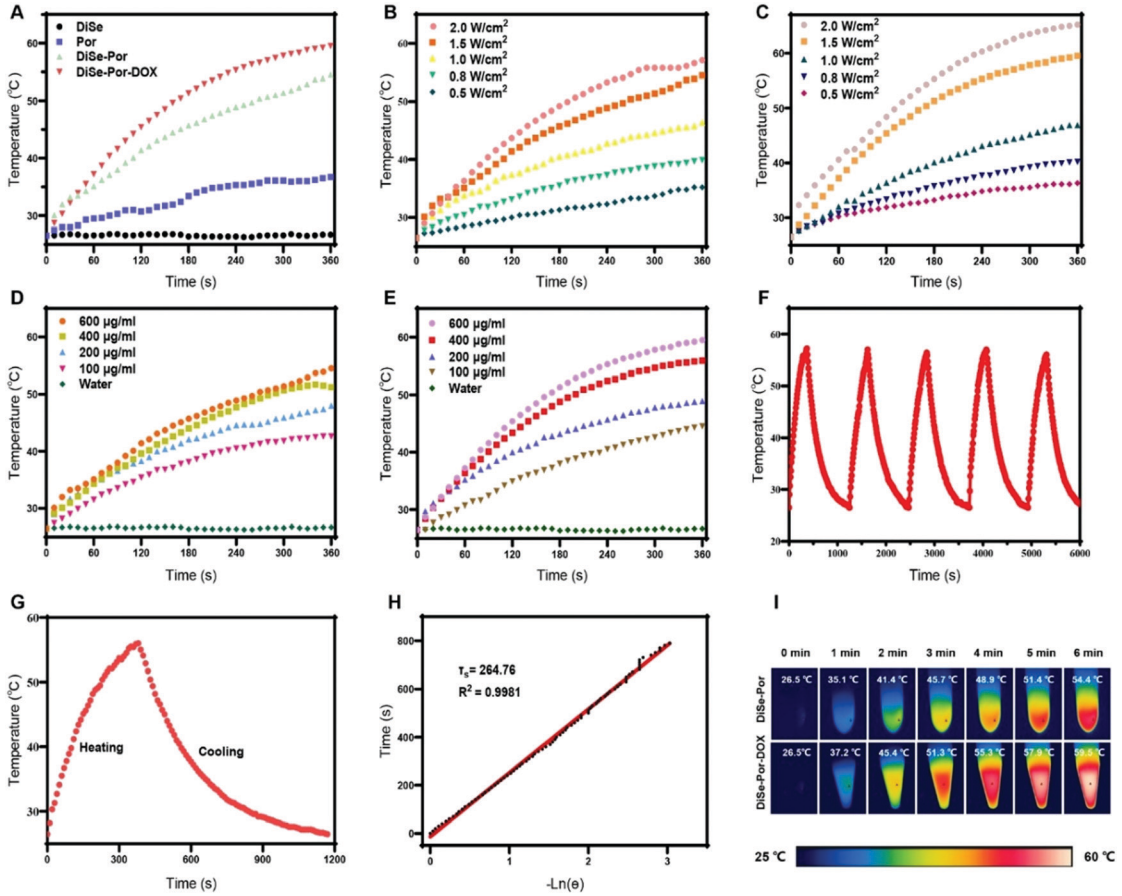

Fig. 2 (A) Temperature evolution of DiSe, Por, DiSe-Por, and DiSe-Por-DOX under 808 nm laser irradiation (600 μg mL^{-1} of DiSe-Por). (B) Power-dependent temperature change of DiSe-Por (600 μg mL^{-1}) under an 808 nm NIR laser. (C) Power-dependent temperature change of DiSe-Por-DOX solutions under irradiation of an 808 nm NIR laser. (D) Concentration-dependent temperature response curves of DiSe-Por at different concentrations under 808 nm irradiation at 1.5 W cm^{-2}. (E) Concentration-dependent temperature response curves of DiSe-Por-DOX solution at different concentrations under 808 nm irradiation at 1.5 W cm^{-2}. (F) Temperature curves of DiSe-Por-DOX under five cycles of photothermal heating by an 808 nm laser at 1.5 W cm^{-2}. (G) Photothermal effect of the aqueous dispersion of DiSe-Por-DOX (400 μg mL^{-1}) under 808 nm laser irradiation (1.5 W cm^{-2}), in which the irradiation lasted to reach the balanceable temperature, and then the laser was shut off. (H) A plot of the cooling period *versus* negative natural logarithm of the temperature. (I) *In vitro* IR thermal photographs of DiSe-Por and DiSe-Por-DOX under NIR laser irradiation taken at a specific time.

expressed GSH in tumor tissues, promoting the release of DOX.[52,53] It could be seen from Fig. 3(B) that in the neutral buffer solution (pH 7.4, GSH 10 mM), the cumulative release reached 69%, 2.5 times higher than that in the buffer solution without GSH (27.9%). To better simulate the tumor microenvironment (acidic pH and high GSH level), we further investigated the release efficiency of DiSe-Por-DOX under the synergistic effect of two stimulating factors. As presented in Fig. 3(C), at a fixed GSH concentration (10 mM), the release amount in acidic media (84.1%) was significantly higher than that in the neutral media (69%). These results suggested that pH and GSH synergize to increase the release of DOX. Furthermore, the thermal responsive release behavior of DiSe-Por-DOX was evaluated by intermittent laser irradiation (Fig. 3(D)). Interestingly, owing to the photothermal activity of DiSe-Por-DOX, the release amount of DOX was further increased after the exposure to laser irradiation. Finally, under the combined action of pH, GSH and photo, the cumulative release amount of DOX reached 89.6% eventually. Overall, the microenvironment of tumor-relevant acidic pH and high GSH level destroyed the skeleton structure of DiSe-Por-DOX, increasing the drug release. The increase in temperature accelerated the movement of drug molecules, promoting the diffusion of the drug from DiSe-Por-DOX.

In vitro cellular uptake

To investigate the internalization behavior of cells to drugs, DiSe-Por-DOX was added to human prostate cancer cells (PC-3) and incubated in different environments for co-culture. And their cellular uptake was observed by inverted fluorescence microscopy.[54] As shown in Fig. 4(A), compared with the weak red fluorescence in the neutral external environment, a strong red fluorescence was observed in the medium similar to the tumor microenvironment. This result demonstrated that the internalized DiSe-Por-DOX was easily decomposed by tumor cells. Noteworthily, such a tendency could also be found from

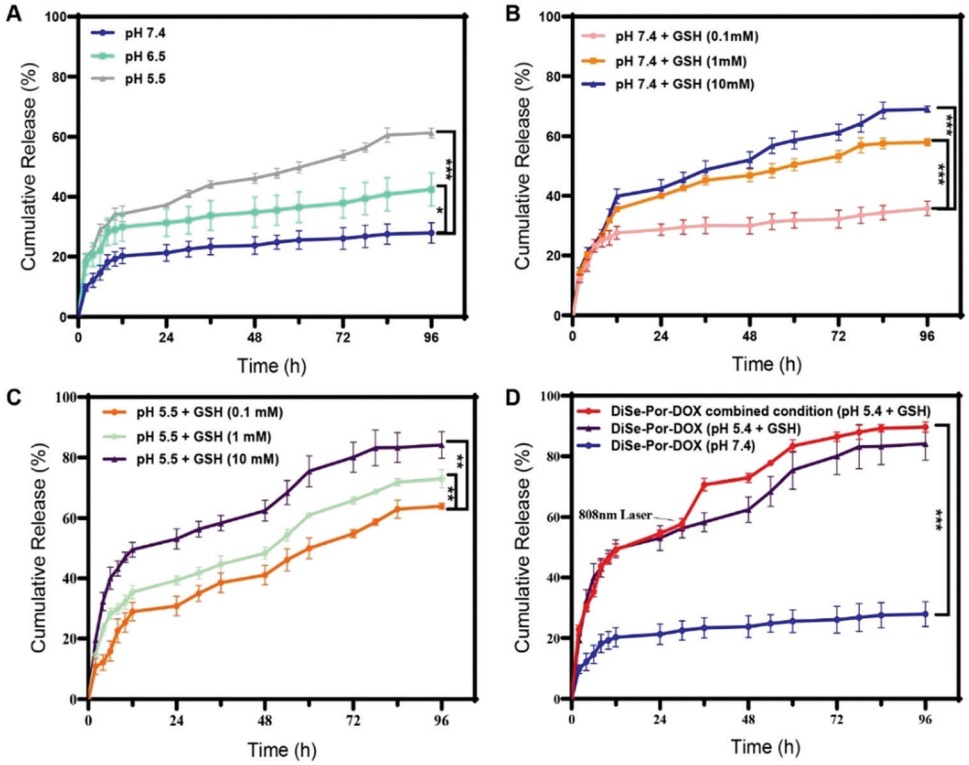

Fig. 3 (A) Cumulative release profiles of DOX from DiSe-Por-DOX in various releasing buffers with different pH values. (B) Cumulative release profiles of DOX from DiSe-Por-DOX in the releasing buffers (pH 7.4) with different concentrations of GSH. (C) Cumulative release profiles of DOX from DiSe-Por-DOX in the releasing buffers (pH 5.5) with different concentrations of GSH. (D) Cumulative release profiles of DOX from DiSe-Por-DOX in releasing buffers that gradually changed the stimulating factors over 96 h. Data are presented as the mean ± SD (n = 3).

the flow cytometry (FC) results shown in Fig. 4(B) and (C). Further TEM observation of the PC-3 cells incubated with DiSe-Por-DOX for 4 h, revealed that the carrier could be internalized into the tumor cells with the appearance of the DiSe-Por-DOX nanosheet in the cytoplasm (Fig. 4(D)). As displayed in Fig. S6 (ESI†), the DOX green signals of DiSe-Por-DOX colocalized with lysosomes over time, which demonstrated that the highly acidic microenvironment of lysosomes favored the drug release process. To further illustrate the tumor-targeting ability of DiSe-Por-DOX, a reverse validation in normal cells (L02 cells and L929 cells) was performed. As shown in Fig. 4(E), strong red fluorescence could be observed in the cells treated with free DOX after incubation for 4 hours. In sharp contrast, only a faint red signal was detected in cells co-incubated with DiSe-Por-DOX even after 6 h. The same trend was also observable in L929 cells (Fig. S7, ESI†). All these results suggested that DiSe-Por-DOX had an excellent passive targeting capacity which could inhibit drug release in the normal physiological environment, overcoming the undifferentiated drug release behavior, and reducing the unnecessary side effects to the human body caused by drugs.

ROS and GSH levels and cell viability study

As an essential trace element in the body, selenium plays an important role in regulating the body's redox and other biological processes.[33] The Se–Se bond could be reduced by the high level of GSH of tumor cells, leading to the generation of ROS detectable by fluorescence probe 2′,7′-dichlorodihydrofluorescein diacetate (DCFH-DA) to generate enhanced green fluorescence.[55] As seen from Fig. 5(A), compared with the PBS group, only a minor change in green fluorescence was detected for the DOX group. Whereas, dramatic enhancement was achieved for the cells treated with DiSe-Por, validating the significant elevation of the ROS level in the tumor cells. After the introduction of DOX to DiSe-Por, a sharp fluorescence enhancement was observed, validating the collaborative amplification of ROS generation combining DOX and DiSe-Por. As shown in Fig. 5(B), the GSH content in cells presented concentration dependence which was decreased with the increase of DiSe-Por. Compared with DOX group (Fig. 5(C)), DiSe-Por-DOX presented a stronger GSH consummation ability. Thereby, the existence of diselenium bond could finely regulate the redox level in the tumor cells, accelerating the release of DOX.

To evaluate the biosafety, blood compatibility was initially studied.[56] As shown in Fig. 5(D), compared with the water group (positive control), the supernatant of RBC suspension was clear with a negligible hemolysis rate (<5%) for DiSe-Por (Fig. S8, ESI†) and DiSe-Por-DOX, revealed the excellent hemocompatibility of both materials. The cytotoxicity was assessed *via* incubation of samples at various concentrations with L02 and L929 cells for 24 h or 48 h. As seen from Fig. S9 (ESI†), DiSe-Por displayed an excellent cyto-compatibility with a negligible

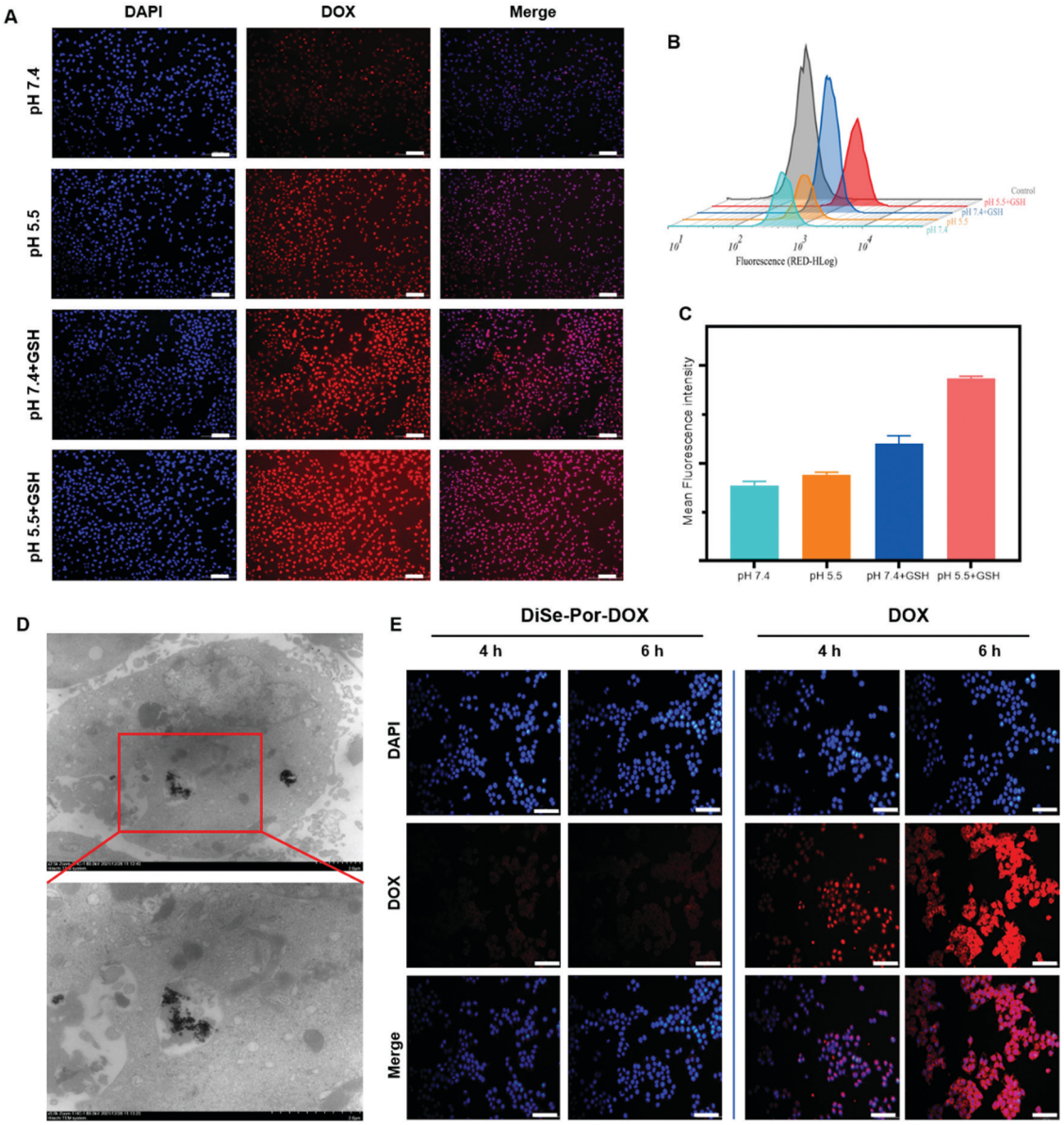

Fig. 4 (A) Fluorescence images of PC-3 cells incubated with DiSe-Por-DOX with different treatments. (B) Corresponding FC examination of cellular uptake and target, FL1-H was chosen to represent the mean FL intensity of PC-3 cells incubated with DiSe-Por-DOX with different treatments and (C) their corresponding MFIs. (D) TEM images of PC-3 cells after incubation with DiSe-Por-DOX for 4 h. (E) Fluorescence images of L02 cells incubated with DiSe-Por-DOX with different treatments (the bar is 100 μm).

cell death even at a high concentration of 200 μg mL^{-1}. Under the same DOX concentration, the survival rate of the cells treated with DiSe-Por-DOX was significantly higher than that of free DOX (Fig. 5(E)).

The photothermal therapeutic efficiency of DiSe-Por *in vitro* was verified by irradiating the tumor cells, which were incubated with DiSe-Por for 12 hours in advance, using a NIR laser (808 nm, 1.5 W cm^{-2}, 5 minutes). The MTT results showed that the cell viability was gradually decreased with the increase of the DiSe-Por concentration (Fig. S10, ESI†), which could be attributed to the existence of the Se–Se bond, promoting the production of ROS in tumor cells. Such a consequence demonstrated that DiSe-Por alone also presented a certain anti-tumor effect *via* chemodynamic therapy.[57] To explore the synergistic anti-tumor effect, PC-3 cells were treated with DOX, DiSe-Por-DOX, and DiSe-Por-DOX + laser (808 nm, 1.5 W cm^{-2}, and 5 min), respectively, with an equivalent drug content for 24 h. As shown in Fig. 5(F), compared with other groups, the DiSe-Por-DOX + laser group, showed the most remarkable antitumor effect. The therapeutic efficacy *in vitro* was further investigated by a live/dead cell staining evaluation through fluorescence microscopy observation. As shown in Fig. 5(G), similar to the cells treated with PBS and PBS + laser, which showed strong green fluorescence, the cells treated with DOX and DOX + laser groups, also showed almost uniform green fluorescence with weak red fluorescence,

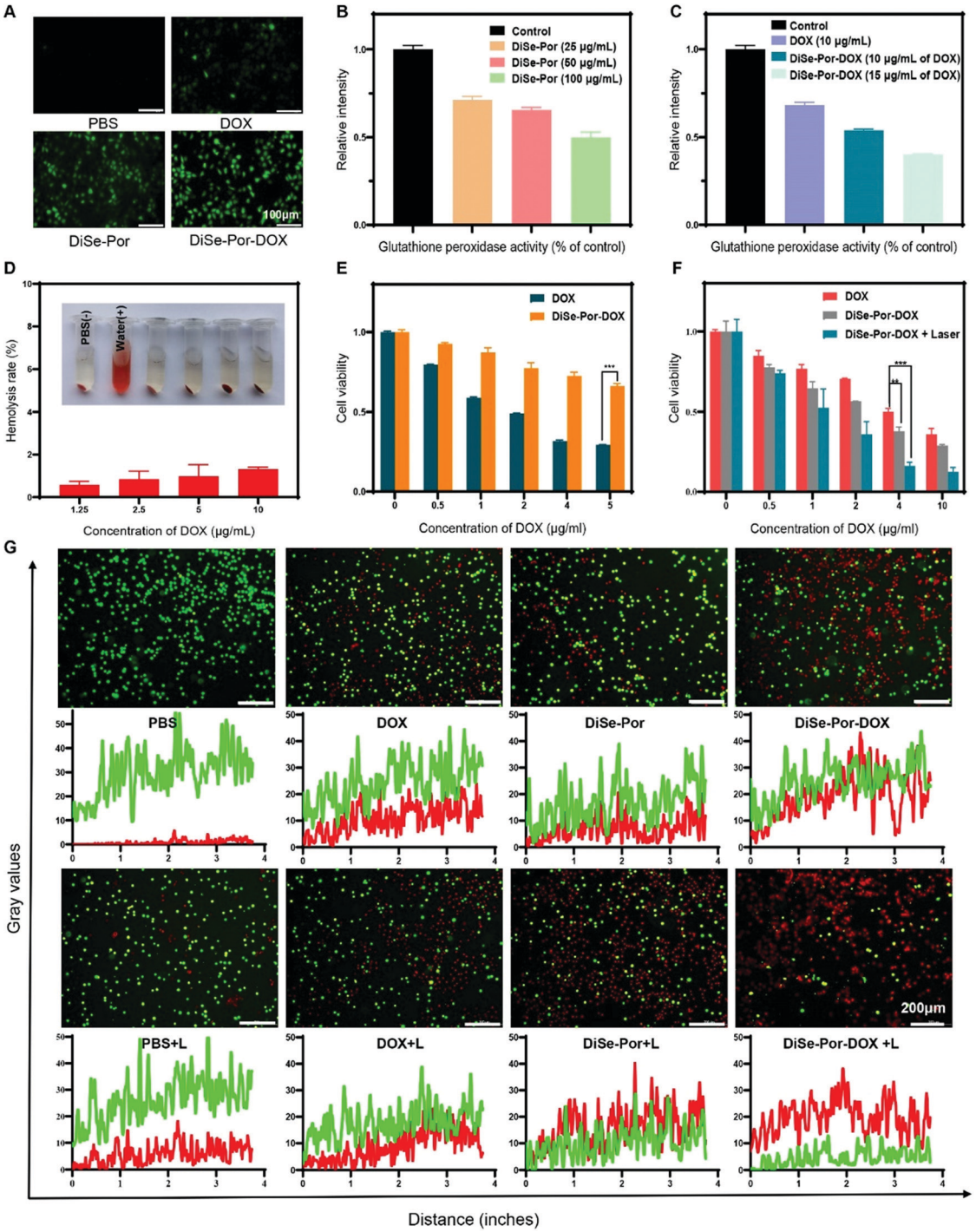

Fig. 5 (A) Inverted fluorescence microscopy images to analyze the intracellular ROS level by DCFH-DA staining after incubation with PBS; DOX; DiSe-Por and DiSe-Por-DOX for PC-3 cells (the concentration of DiSe-Por is 100 μg mL^{-1}). The scale bar is 100 μm. Intracellular GSH levels of PC-3 cells treated with (B) DiSe-Por, (C) DOX, and DiSe-Por-DOX, respectively. (D) Hemolysis ratio and images of RBCs treated with DiSe-Por-DOX of different concentrations. (E) *In vitro* cell viabilities of L02 cells treated with DOX and DiSe-Por-DOX in various concentrations. (F) Cell viability of PC-3 treated with DOX, DiSe-Por-DOX, and DiSe-Por-DOX + laser (808 nm, 1.5 W cm^{-2}, and 5 min) with various concentrations (*$P < 0.05$, **$P < 0.01$, ***$P < 0.001$). (G) Fluorescence images of PC-3 cells under different treatments, in which live and dead PC-3 cells were co-stained with Calcein-AM and propidium iodide. The scale bar is 200 μm.

indicating that there was no further therapeutic effect after laser irradiation. Compared with the DOX group, the DiSe-Por-DOX group presented strong red fluorescence, demonstrating a better anti-tumor effect of DiSe-Por-DOX. However, upon illumination, the DiSe-Por and DiSe-Por-DOX groups presented an obvious red signal, revealing that the

therapeutic effect could be significantly improved through the exertion of PTT.

Pharmacokinetics, biodistribution and thermal imaging

The biodistribution and tumor targeting ability were investigated by determining the fluorescence signal of DOX in tumors and organs *via* the small animal imaging system. The mice were sacrificed and their tumors, and the major organs were removed at different time points for fluorescence detection. As shown in Fig. 6(A) and (B), both DOX and DiSe-Por-DOX were accumulated in tumors and reached the maximum value at 12 h post-injection. Whereas, compared to free DOX, the DOX accumulation amount of DiSe-Por-DOX was higher in the tumor regions, which could be ascribed to the site-specific drug release behavior of DiSe-Por-DOX in the tumor site. Meanwhile, DOX signals could be detected in various exposed organs and tumors within 24 h after intravenous injection. Compared with free DOX, the stronger red signal indicated a longer blood circulation time and higher tumor accumulation of DiSe-Por-DOX. The pharmacokinetics of the drug loading system was evaluated by detecting the changes in the DOX concentration in blood at different times after the tail vein injection.[58] As shown

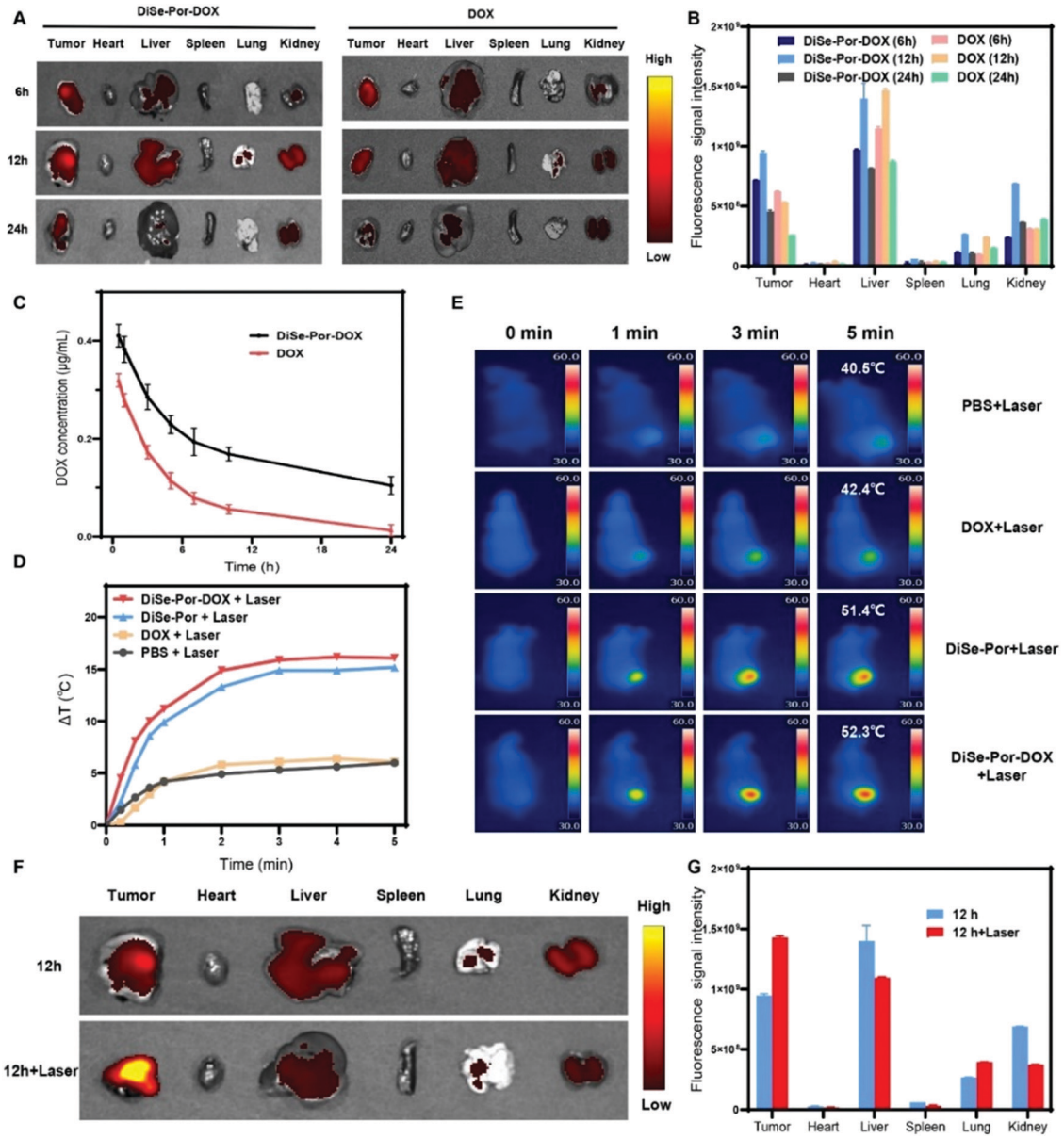

Fig. 6 (A) *Ex vivo* fluorescence images and (B) fluorescence intensity of major organs, and tumors sacrificed from tumor bearing mice after being injected with DiSe-Por-DOX solutions and free DOX at different times. (C) Pharmacokinetics of DiSe-Por-DOX and free DOX from tumor-bearing mice after intravenous injection. (D) Temperature changes and (E) thermographic images of the tumor area of the mice treated with saline, DOX, DiSe-Por and DiSe-Por-DOX after 5 min of laser exposure. (F) *Ex vivo* fluorescence images and (G) fluorescence intensity of major organs, and tumors sacrificed from tumor bearing mice after different treatments.

in Fig. 6(C), the blood DOX concentration decreased rapidly for the pure DOX group, which was significantly lower than the DiSe-Por-DOX group at the same time point. The single compartment model was adopted to calculate the half-life, and the results showed the half-life of DiSe-Por-DOX was 12.4 h and free DOX group half-life was 5.4 h. DiSe-Por-DOX half-life extension was about 2.3 times that of free DOX. Such a consequence further indicated that the clearance of plasma DOX in the composite was considerably delayed and the circulation time in the body was effectively prolonged, which was beneficial for drug accumulation in the tumor site.

To explore the photothermal properties *in vivo*, PBS, DOX, DiSe-Por and DiSe-Por-DOX were intravenously injected into the mice bearing PC-3 tumor. The temperature of tumor site was monitored by an infrared thermal camera at 12 h post-injection after 5 min of laser irradiation. In contrast to the slight increase in the PBS and DOX groups, the mice injected with DiSe-Por-DOX, showed a prompt temperature increase on the tumor sites which was higher than that of the DiSe-Por. It reached nearly 51 °C after irradiation for 3 min, which could effectively kill the tumor cells *in vivo* (Fig. 6(D) and (E)). The enhancement of the drug release caused by the PTT was verified by detecting drug fluorescence inside the tumor *via* small animal imaging *in vivo*. As shown in Fig. 6(F) and (G), owing to the accelerated movement of drug molecules caused by high temperature, the fluorescence intensity of tumor tissues with laser irradiation was much stronger than the unilluminated group.

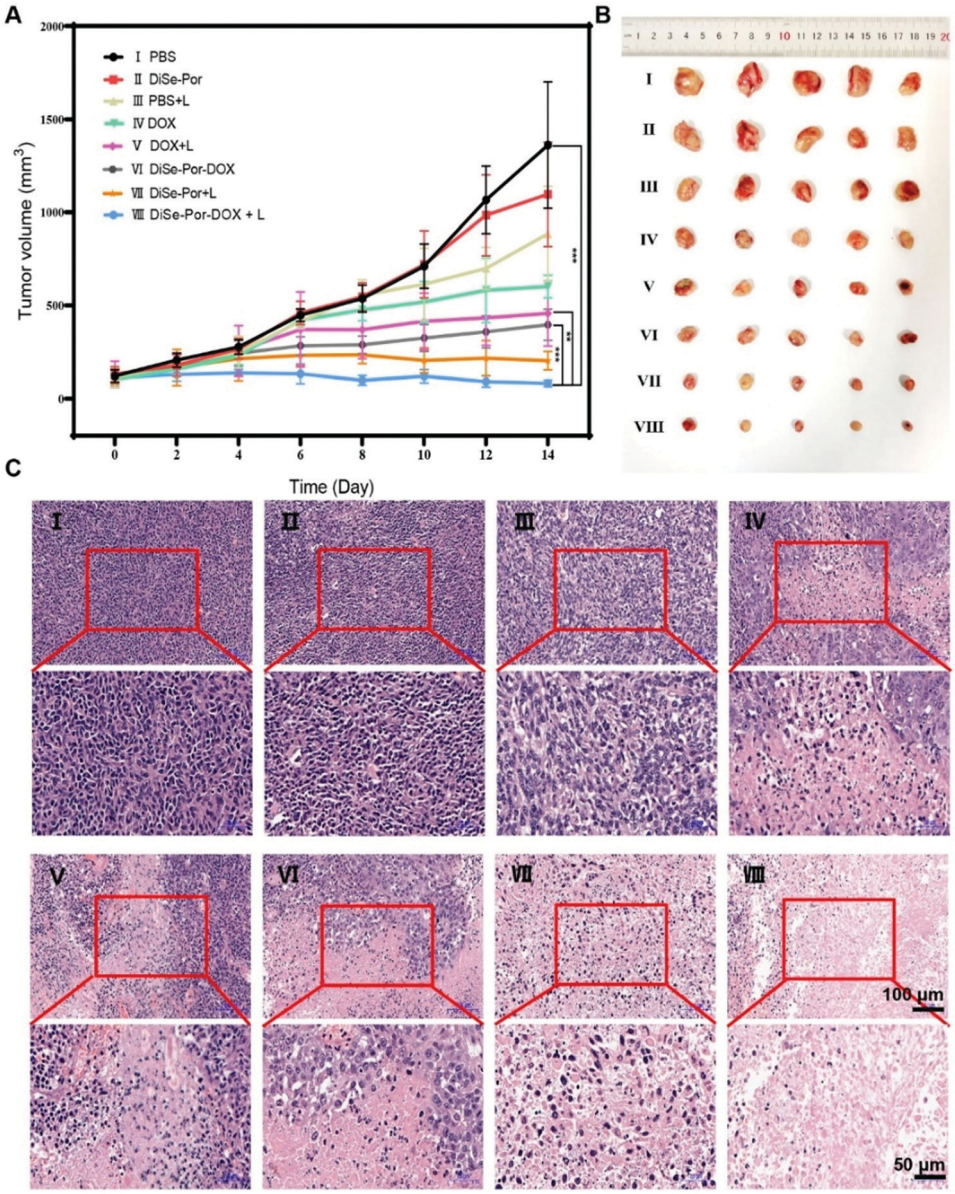

Fig. 7 (A) Tumor volume changes in 14 days. (B) Photographs of the excised tumors after 14 days of treatment. (C) H&E staining of tumor tissues at the 14th day.

Anticancer effect *in vivo*

The combined therapeutic efficacy of DiSe-Por-DOX *in vivo* was evaluated using PC-3 tumor xenografted mice. According to the *in vivo* IVIS fluorescence imaging, the irradiation (808 nm, 1.5 W cm^{-2}, and 5 min) was conducted 12 h post-injection. Following irradiation, both the body weight and tumor size were measured every 2 days. Similar to the PBS group, a fast tumor increase was observed for the mice treated with DiSe-Por, indicating that DiSe-Por alone was insufficient to kill tumor cells. The tumor growth of the DOX containing groups, including DOX, DOX + laser, and DiSe-Por-DOX, was inhibited to a certain extent, whereas the growth of tumors in the DiSe-Por and DiSe-Por-DOX groups was significantly suppressed after laser irradiation. The combination therapy for DiSe-Por-DOX + laser irradiation resulted in the most significant inhibition of tumor growth compared to other groups, suggesting an enhanced *in vivo* combinative antitumor therapy (Fig. 7(A) and (B)). Similarly, the super synergistic chemo/photothermal/chemodynamic antitumor effect of DiSe-Por-DOX could also be validated by the change of tumor weight (Fig. S12, ESI†). Not only the tumor sizes were the assessment indicator of the tumor treatment effect, but the histologic analysis could also explain the extent of dead cancer cells. The tumors of all the groups were removed after a 14 day treatment, which were ready for H&E histological analysis (Fig. 7(C)). The tumor cells grew quickly with no sign of necrosis in the PBS, DiSe-Por, and PBS + laser groups. By contrast, in the tumor site of other groups, an extensive necrosis area was apparently stained by eosin. Moreover, over 95% of necrotic cancer cells were dyed by eosin in the tri-therapy group.[59] The results of H&E histological analysis were consistent with the tumor suppressive effect. During the whole experiment, the average weight of all mice increased slightly, indicating a good biological safety (Fig. S13, ESI†) of the COF carrier. Additionally, the pathomorphological analysis results indicated that there were no obvious lesions (Fig. S14, ESI†), which further implied the low *in vivo* toxicity of the drug delivery system.

Conclusion and discussion

A novel joint photothermal–chemo–chemodynamic therapy applying the pH/GSH/photo triple-responsive COF drug carriers was developed. The well-designed DiSe-Por-DOX could effectively accumulate in the tumor sites. After being internalized by tumor cells, the specific microenvironment of cancer cells, *i.e.* the acidic pH and high intracellular GSH level, triggered the breaking of imine and Se–Se bonds, accelerating the release of DOX, which could penetrate deep into tumor tissue for rapid killing of cancer cells. And the breaking of Se–Se bonds induced the generation of ROS in tumor cells, which further broke the intracellular redox/oxidation state balance. The release of DOX in the tumor sites could be further amplified by external NIR irradiation. Under the combined action of pH, GSH and photo irradiation, the cumulative release amount of DOX reached 89.6% eventually for DiSe-Por-DOX. Consequently, the synergistic therapy could make each therapy exert the maximum effect, achieving the best treatment effect. All human prostate cancer (PC-3) xenografted in nude mice could be greatly inhibited with approximately 93.5% of the tumors being completely eradicated. Furthermore, the biosafe DiSe-Por could greatly reduce the toxicity of DOX. These results revealed the huge application potential of the joint photothermal–chemo–chemodynamic therapy based on the triple-stimuli-responsive COF-DOX drug delivery system for efficient tumor treatment.

Conflicts of interest

The authors declare that they have no competing interests.

Acknowledgements

This work was supported by the Shandong Province Natural Science Foundation (ZR2020QB067).

References

1 R. L. Siegel, K. D. Miller, H. E. Fuchs and A. Jemal, *Ca-Cancer J. Clin.*, 2021, **71**, 7–33.
2 X. Hou, Y. Tao, Y. Pang, X. Li, G. Jiang and Y. Liu, *Int. J. Cancer*, 2018, **143**, 3050–3060.
3 C. Ning, J. Jiajia, L. Meng, Q. Hongfei, W. Xianglong and L. Tingli, *Mater. Sci. Eng., C*, 2019, **104**, 109746.
4 Z. Xie, T. Fan, J. An, W. Choi, Y. Duo, Y. Ge, B. Zhang, G. Nie, N. Xie, T. Zheng, Y. Chen, H. Zhang and J. S. Kim, *Chem. Soc. Rev.*, 2020, **49**, 8065–8087.
5 S. Gao, T. Li, Y. Guo, C. Sun, B. Xianyu and H. Xu, *Adv. Mater.*, 2020, **32**, e1907568.
6 S. Zhou, D. Li, C. Lee and J. Xie, *Trends Chem.*, 2020, **2**, 1082–1095.
7 B. Kalyanaraman, *Redox Biol.*, 2020, **29**, 101394.
8 A. Ogden, P. C. Rida, B. S. Knudsen, O. Kucuk and R. Aneja, *Cancer Lett.*, 2015, **367**, 89–92.
9 V. Bala, S. Rao, B. J. Boyd and C. A. Prestidge, *J. Controlled Release*, 2013, **172**, 48–61.
10 B. B. Zhou, H. Zhang, M. Damelin, K. G. Geles, J. C. Grindley and P. B. Dirks, *Nat. Rev. Drug Discovery*, 2009, **8**, 806–823.
11 A. K. Iyer, A. Singh, S. Ganta and M. M. Amiji, *Adv. Drug Delivery Rev.*, 2013, **65**, 1784–1802.
12 D. J. Irvine and E. L. Dane, *Nat. Rev. Immunol.*, 2020, **20**, 321–334.
13 J. Walker and B. W. Loo, Jr., *JAMA Oncol.*, 2019, **5**, 1291–1292.
14 D. Salas-Benito, J. L. Pérez-Gracia, M. Ponz-Sarvisé, M. E. Rodriguez-Ruiz, I. Martínez-Forero, E. Castañón, J. M. López-Picazo, M. F. Sanmamed and I. Melero, *Cancer Discovery*, 2021, **11**, 1353–1367.
15 H. Lou, H. Fang, T. Wang, D. Wang, Q. Han, W. Zhou, Y. Song, W. Tan and B. Zhou, *ACS Appl. Polym. Mater.*, 2022, **4**, 714–724.
16 B. Wang, A. R. Warden and X. Ding, *Drug Discovery Today*, 2021, **26**, 2646–2659.

17 T. A. Yap, E. E. Parkes, W. Peng, J. T. Moyers, M. A. Curran and H. A. Tawbi, *Cancer Discovery*, 2021, **11**, 1368–1397.
18 Z. Yu, Y. Hu, Y. Sun and T. Sun, *Chem. – Eur. J.*, 2021, **27**, 13953–13960.
19 B. Ma and A. Bianco, *Small*, 2021, **17**, 2102557.
20 N. Singh, S. Son, J. An, I. Kim, M. Choi, N. Kong, W. Tao and J. S. Kim, *Chem. Soc. Rev.*, 2021, **50**, 12883–12896.
21 P. Wang, M. Xiao, H. Pei, H. Xing, S.-H. Luo, C.-K. Tsung and L. Li, *Chem. Eng. J.*, 2021, **415**, 129036.
22 J. Dai, Y. Su, S. Zhong, L. Cong, B. Liu, J. Yang, Y. Tao, Z. He, C. Chen and Y. Jiang, *Signal Transduction Targeted Ther.*, 2020, **5**, 145.
23 I. K. Herrmann, M. J. A. Wood and G. Fuhrmann, *Nat. Nanotechnol.*, 2021, **16**, 748–759.
24 A. Madni, R. Kousar, N. Naeem and F. Wahid, *J. Bioresour. Bioprod.*, 2021, **6**, 11–25.
25 B. Joseph, V. Sagarika, C. Sabu, N. Kalarikkal and S. Thomas, *J. Bioresour. Bioprod.*, 2020, **5**, 223–237.
26 X. Chen, K. Geng, R. Liu, K. T. Tan, Y. Gong, Z. Li, S. Tao, Q. Jiang and D. Jiang, *Angew. Chem., Int. Ed.*, 2020, **59**, 5050–5091.
27 J. L. Segura, S. Royuela and M. Mar Ramos, *Chem. Soc. Rev.*, 2019, **48**, 3903–3945.
28 A. Murali, G. Lokhande, K. A. Deo, A. Brokesh and A. K. Gaharwar, *Mater. Today*, 2021, **50**, 276–302.
29 S. Bhunia, K. A. Deo and A. K. Gaharwar, *Adv. Funct. Mater.*, 2020, **30**, 2002046.
30 S. Kandambeth, K. Dey and R. Banerjee, *J. Am. Chem. Soc.*, 2019, **141**, 1807–1822.
31 C. Zheng, M. Li and J. Ding, *BIO Integr.*, 2021, **2**, 57–60.
32 L. V. Yang, *Int. J. Mol. Sci.*, 2017, **18**, 2729.
33 K. Lossow, M. Schwarz and A. P. Kipp, *Redox Biol.*, 2021, **42**, 101900.
34 A. Esrafili, A. Wagner, S. Inamdar and A. P. Acharya, *Adv. Healthcare Mater.*, 2021, **10**, e2002090.
35 S. Mura, J. Nicolas and P. Couvreur, *Nat. Mater.*, 2013, **12**, 991–1003.
36 D. Singh, A. M. Deobald, L. R. Camargo, G. Tabarelli, O. E. Rodrigues and A. L. Braga, *Org. Lett.*, 2010, **12**, 3288–3291.
37 Y. Yi, S. Fa, W. Cao, L. Zeng, M. Wang, H. Xu and X. Zhang, *Chem. Commun.*, 2012, **48**, 7495–7497.
38 M. Z. Kassaee, E. Motamedi, B. Movassagh and S. Poursadeghi, *Synthesis*, 2013, 2337–2342.
39 Y. Lu, J. Zhang, W. Wei, D. D. Ma, X. T. Wu and Q. L. Zhu, *ACS Appl. Mater. Interfaces*, 2020, **12**, 37986–37992.
40 M. Keyhaniyan, A. Shiri, H. Eshghi and A. Khojastehnezhad, *New J. Chem.*, 2018, **42**, 19433–19441.
41 K. Songsurang, N. Praphairaksit, K. Siraleartmukul and N. Muangsin, *Arch. Pharmacal Res.*, 2011, **34**, 583–592.
42 K. Wang, Z. Zhang, L. Lin, K. Hao, J. Chen, H. Tian and X. Chen, *ACS Appl. Mater. Interfaces*, 2019, **11**, 39503–39512.
43 X. Xiang, H. Pang, T. Ma, F. Du, L. Li, J. Huang, L. Ma and L. Qiu, *J. Nanobiotechnol.*, 2021, **19**, 92.
44 M. Nosan, M. Löffler, I. Jerman, M. Kolar, I. Katsounaros and B. t Genorio, *ACS Appl. Energy Mater.*, 2021, **4**, 3593–3603.
45 B. Zhou, F. Yan, X. Li, J. Zhou and W. Zhang, *ChemSusChem*, 2019, **12**, 915–923.
46 J. Dou, M. Qi, H. Wang, W. Shi, X. Luan, W. Guo, L. Xiao, C. Zhao, D. Cheng, T. Jiang, W. Zhang, W. Bian and B. Zhou, *Microporous Mesoporous Mater.*, 2021, **320**, 111101.
47 Z. Xu, L. Hu, J. Ming, X. Cui, M. Zhang, J. Dou, W. Zhang and B. Zhou, *Microporous Mesoporous Mater.*, 2020, **303**, 110259.
48 F. Hu, W. Li, M. Zou, Y. Li, F. Chen, N. Lin, W. Guo and X. Y. Liu, *ACS Nano*, 2021, **15**, 9559–9567.
49 Z. Liu, A. C. Fan, K. Rakhra, S. Sherlock, A. Goodwin, X. Chen, Q. Yang, D. W. Felsher and H. Dai, *Angew. Chem., Int. Ed.*, 2009, **48**, 7668–7672.
50 Q. Guan, L. L. Zhou, Y. A. Li, W. Y. Li, S. Wang, C. Song and Y. B. Dong, *ACS Nano*, 2019, **13**, 13304–13316.
51 D. Wang, Z. Zhang, L. Lin, F. Liu, Y. Wang, Z. Guo, Y. Li, H. Tian and X. Chen, *Biomaterials*, 2019, **223**, 119459.
52 C. Luo, J. Sun, D. Liu, B. Sun, L. Miao, S. Musetti, J. Li, X. Han, Y. Du, L. Li, L. Huang and Z. He, *Nano Lett.*, 2016, **16**, 5401–5408.
53 N. Yang, W. Xiao, X. Song, W. Wang and X. Dong, *Nano-Micro Lett.*, 2020, **12**, 15.
54 R. Fan, C. Chen, H. Hou, D. Chuan, M. Mu, Z. Liu, R. Liang, G. Guo and J. Xu, *Adv. Funct. Mater.*, 2021, **31**, 2009733.
55 J. Hartwig, M. Loebel, S. Steiner, S. Bauer, Z. Karadeniz, C. Roeger, C. Skurk, C. Scheibenbogen and F. Sotzny, *Front. Immunol.*, 2021, **12**, 581799.
56 L. Zhao, M. Jiang, Z. Xu, F. Sun, X. Wu, M. Zhang, X. Guan, J. Ma and W. Zhang, *J. Colloid Interface Sci.*, 2022, **605**, 752–765.
57 D. Radomska, R. Czarnomysy, D. Radomski and K. Bielawski, *Int. J. Mol. Sci.*, 2021, **22**, 1009.
58 C. A. Ferreira, S. Goel, E. B. Ehlerding, Z. T. Rosenkrans, D. Jiang, T. Sun, E. Aluicio-Sarduy, J. W. Engle, D. Ni and W. Cai, *Nano Lett.*, 2021, **21**, 4692–4699.
59 H. Zhang, X.-T. Tian, Y. Shang, Y.-H. Li and X.-B. Yin, *ACS Appl. Mater. Interfaces*, 2018, **10**, 28390–28398.

